



Coupled three dimensional DEM–CFD simulation of a lime shaft kiln—Calcination, particle movement and gas phase flow field

Bastian Krause*, Birk Liedmann, Jens Wiese, Siegmar Wirtz, Viktor Scherer

Department of Energy Plant Technology (LEAT), Ruhr-University Bochum, Universitätsstraße 150, 44780 Bochum, Germany



HIGHLIGHTS

- 3D simulation of a shaft kiln for limestone conversion.
- Coupled DEM/CFD model to describe effects on kiln and particle scale.
- Distinct temperature gradients in the polydisperse limestone bed.
- Distinct temperature and gas concentration gradients in the particles.
- Transport mechanisms in the limestone affect the kiln behavior.

ARTICLE INFO

Article history:

Received 29 January 2015

Received in revised form

22 April 2015

Accepted 2 June 2015

Available online 9 June 2015

Keywords:

Shaft kiln

Discrete Element Method

CFD

Heat transfer

Calcination

Granular material

ABSTRACT

In lime shaft kilns the limestone is heated in counterflow with the flue gas from multiple burners, commonly fired by fossil or alternative fuels. After preheating, the limestone enters the calcination zone with gas temperatures above approximately 900 °C. To achieve high thermal efficiencies and calcination degrees, a homogeneous gas flow through the packed bed is essential. Spatial pressure differences and energy sinks and sources resulting from the calcination process and the fuel combustion make it even more difficult to predict the actual three-dimensional temperature and flow distribution in the kiln. Furthermore the particle size distribution is important for the system design, because limestone with larger size needs significantly higher residence time in the calcination zone for full conversion.

This work presents the application of a novel 3-dimensional particle-mechanics based, numerical tool on an industrial scale. The tool allows the simulation of a moving and reacting limestone bed in a shaft kiln coupled with the 3-dimensional CFD-simulation describing the interstitial gas phase. Convective heat transfer between gas phase and particles, radiative and contact heat transfer between particles as well as calcination reaction are accounted for. With this combined approach the calcination of the limestone bed can be simultaneously described on the system scale while resolving detailed thermo-chemical processes on the particle scale.

© 2015 Published by Elsevier Ltd.

1. Introduction

In lime industry natural limestone is taken from a quarry and crushed to particles of several centimeters size. During the subsequent calcination process the main limestone component calcium carbonate is dissociated at high temperatures into calcium oxide and carbon dioxide (Stark and Wicht, 2000). In vertical lime shaft kilns the heat of reaction required for this endothermic process is supplied via combustion. Due to the comminution process the bed is characterized by a broad grain size distribution,

thus decomposition times of the individual particles can vary considerably. The calcination reaction front advances from the particle surface to the center and the rate-determining steps are mainly the heat transport from the surrounding gas phase to the reaction front and the diffusional mass transfer of the released CO₂ to the gas phase. The optimal operating point of a shaft kiln aims at an almost complete calcination of the entire particle bed and therefore, an almost uniform radial temperature distribution in the kiln and thus a long calcination zone.

Recent work by other authors mainly dealt with one-dimensional approaches for the simulation of lime shaft kilns (Shagapov and Burkin, 2008; Bes, 2006; Senegačnik et al., 2008). In recent years the DEM-CFD coupling approach has become a valuable tool for simulations of reactors processing granular materials. Examples are simulations of rotary kilns (Shi et al.,

* Correspondence to: Department of Energy Plant Technology (LEAT), Ruhr-University Bochum, Universitätsstr. 150, Building IC 2/95, D-44780 Bochum, Germany. Tel.: +49 234 32 26334; fax: +49 234 32 14358.

E-mail address: krause@leat.rub.de (B. Krause).

2008; Amritkar et al., 2014), grate firing systems (Peters and Džiugys, 2014; Simsek et al., 2009), drying of granular materials (Mahmoudi et al., 2014; Sudbrock et al., 2015) or pyrolysis of biomass in packed bed reactors (Mahmoudi et al., 2014; Copertaro et al., 2015). Bluhm-Drenhaus et al. Bluhm-Drenhaus et al. (2010) presented a three-dimensional coupled DEM–CFD simulation of a scaled lime shaft kiln using a shrinking core approach to describe the particle calcination. Instead of modeling the fuel combustion in bed a simplified approach using a source term for the supply of thermal energy has been applied. Based on this previous work the model approach has been extended in the work described in the current paper. A coupled DEM–CFD simulation of an industrial scale kiln taking into account the fuel combustion in the gas phase is presented. In addition an improved numerical particle model has been implemented describing the inner particle thermo-chemical processes for a wide range of particle sizes.

2. The simulation procedure

The DEM code developed at the Department of Energy Plant Technology (Kruggel-Emden et al., 2007; Simsek et al., 2008) describes the particle motion and thermo-chemical processes of the reacting granular phase. The commercial CFD software package ANSYS FLUENT (Version 14.5) is used to solve the governing equations of the fluid phase.

In this paper a quasi steady-state simulation is discussed aiming at the steady state operation of a shaft kiln characterized by constant inlet and outlet conditions. The simulation is conducted in two stages. The first stage computes the particle motion independent from thermo-chemical processes and fluid flow (see Section 2.3). In the second stage these effects are included in a coupled simulation of particle conversion and fluid flow. Therefore the DEM simulation from stage one provides the particle positions and velocities. This separation is possible since both thermochemical processes and fluid flow have a negligible influence on the movement of the particle bed. The velocity of the gas phase (see Fig. 10) is too low for a significant acceleration of limestone particles and therefore particle trajectories are not influenced by gas phase drag forces. Furthermore the calcination reaction does not affect the particle diameter significantly, because the particle mass loss due to the released CO₂ is accompanied by an increasing inner particle porosity (Stark and Wicht, 2000). Thus the particle motion can be described independently and the two stages can be computed sequentially. The advantage of this two-staged scheme is a considerable saving of computational resources, since the DEM simulation of particle movement needs much smaller time steps than the coupled simulation and therefore consumes significantly more computing time. Using this approach a coupled simulation of the shaft kiln (stage two) does not require more than three days computational time (on mainstream hardware – dual CPU – 4 × 2,5 GHz, 16 GB DDR3 Ram), allowing parameter variations for different operational modes of the shaft kiln.

2.1. Particle and fluid phase coupling

Particle and gas phase interact with each other by exchanging mass, momentum and energy, thereby several quantities have to be transferred from DEM to CFD and vice versa. Hence, the interaction between the particle and fluid phase in cases of heat and mass transfer is implemented as a two-way coupling. Note that the coupling between fluid flow and particle movement is “one way”, because particle movement is not influenced by drag forces as already mentioned. On both sides (DEM and CFD) different mesh types are used. The computational background grid for the DEM simulation is an orthogonal, cartesian type with a

mesh size prescribed by the largest particle diameter. In contrast, the CFD mesh is unstructured and non-orthogonal. Due to the different grid types a mass and energy conserving interpolation and data exchange procedure between the discrete particulate phase and the continuous fluid phase is essential.

Bluhm-Drenhaus et al. (2010) introduced an orthogonal transfer mesh with a resolution much finer than the fluid mesh to provide interpolation and integration points for the data transfer between particle positions and the CFD mesh and vice versa (see Fig. 1). The DEM side computes volume-averaged and linearized source terms of energy and mass, the transfer to the CFD code is carried out by a “particle source in cell” approach (Crowe et al., 1977). Based on a particle's position its spatial extent is associated with the transfer mesh. The volumetric source terms of a CFD cell are defined by integration over those transfer cells, which are geometrically located inside the CFD cell. This communication direction is visualized in the upper section of Fig. 1. Concurrently to the DEM computations a CFD simulation step solves the fluid phase continuum equations (see Section 2.2), taking into account the source terms received from DEM, and returns gas temperatures, velocities and fluid properties of each CFD cell to the corresponding cells of the transfer mesh. This is the reciprocal communication direction visualized in the lower section of Fig. 1. Particle boundary conditions are determined from the transfer cell containing the particle's center of gravity. This implies the assumption that changes in fluid properties are negligible with regard to the particle scale. The coupling method is described in more detail in (Rickelt et al., 2013).

2.2. The fluid phase

The determination of the local velocity field around each individual particle in a bed with a low permeability and the dimension of a shaft kiln is computationally far too expensive (Nijemeisland et al., 2004). As a common approach to make large scale industrial reactor simulations feasible the fixed bed is handled as a porous medium (Fluent, 2012; Jakobsen et al., 2002) and the influence of local fluctuations is modeled on a sub-grid scale in the context of pressure drop (Ergun equation) and heat transfer submodels (see Section 2.3.1). In order to describe the surrounding fluid phase the standard main governing equations of the one-temperature porous medium model as implemented in ANSYS FLUENT are used. The additional resistance to the flow caused by the physical presence of the solid phase is modeled as an extra term in the momentum balance equation (S_{int}). This term is provided by the Ergun equation (Eq. (1)) which consists of a viscous and inertial pressure loss

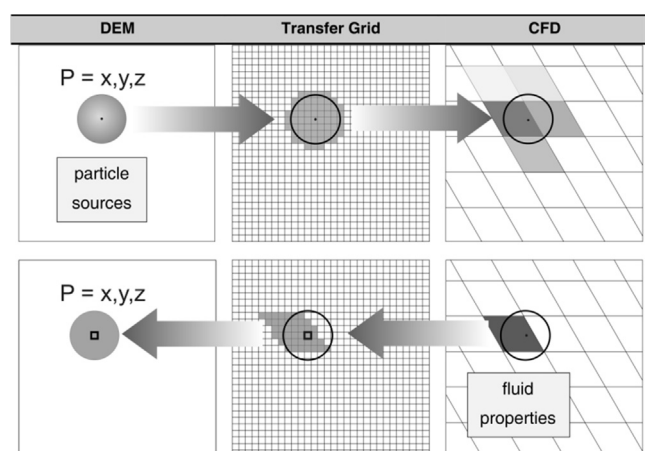
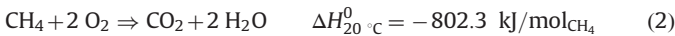


Fig. 1. Interconnection through transfer cells (Rickelt et al., 2013).

term, depending on the superficial fluid velocity v_f , the void fraction ϕ , the fluid density ρ_f and dynamic viscosity μ_f .

$$\vec{S}_{int} = 150 \cdot \frac{(1-\phi)^2 \cdot \mu_f}{d_{h,p}^2 \cdot \phi^2} \cdot \vec{v}_f + 1.75 \cdot \frac{\rho_f \cdot (1-\phi) \cdot |\vec{v}_f|}{d_{h,p} \cdot \phi} \cdot \vec{v}_f \quad (1)$$

For a monodisperse bed the hydraulic diameter $d_{h,p}$ is equal to the particle diameter and for a polydisperse bed to the Sauter mean diameter. The void fraction ϕ of the particle bed is determined by the previous DEM simulation of the particle movement in the lime shaft kiln. Note that the macroscopic flow in the kiln is assumed to be laminar because the resolution of the CFD mesh cannot resolve the effect of turbulence in the cavities between particles. The lime shaft kiln is fired by methane injected at about 50% kiln height (see Fig. 7). The methane combustion is modeled on the CFD side with the standard “one-step methane/air combustion” using an Arrhenius rate expression for the description of the conversion rate (Eqs. (2) and (3)).



$$r_{\text{CH}_4} = A_{r,m} \cdot \exp\left(\frac{E_{r,m}}{R \cdot T_f}\right) \cdot c_{\text{CH}_4}^{0.1} \cdot c_{\text{O}_2}^{1.65} \quad (3)$$

Here the pre-exponential factor is $A_{r,m}=6.186 \cdot 10^9$ and the activation energy is $E_{r,m}=125.6 \text{ kJ/mol}$. The calcination reaction and the release of CO_2 into the gas phase are taken into account on the DEM-side. This submodel is presented in Section 2.3.3. Analogously the convective heat transfer, mass and species transfer between the phases is included. The convective heat transfer between the two phases is included by an energy source term in the gas-phase energy equation (CFD sided). In the same way mass and species transfer between the phases is included by a mass source term in the species conservation equation (CFD sided). In particular the mass transfer of CO_2 released from the particulate phase to the fluid phase is a substantial process and must be considered.

2.3. The particle phase: particle motion

The mechanically induced particle motion is described with the Discrete Element Method (DEM) (Cundall and Strack, 1979). A major simplification is the assumption that limestone particles are of spherical shape. This simplification is justified to a certain extent by the fact that the shape of typical crushed limestone particles is not totally different from spheres. In addition the particles are smoothed and rounded due to mechanical interactions in the limestone bed and hence approach a spherical shape. The consideration of complex particle shape would have led to an unacceptable computational effort. The translational and rotational movement of each particle is calculated by solving Newton's (Eq. (4)) and Euler's equations (Eq. (5)) of motion. Due to the moderate gas velocities, gravity and contact forces are predominant in the system and the effect of interaction forces between the fluid and the particles can be neglected on the DEM-side, leading to the following expressions.

$$m_i \cdot \frac{d^2 \vec{x}_i}{dt^2} = \sum_{j=1}^N \vec{F}_{ij} + m_i \cdot \vec{g} = \vec{F}_i + m_i \cdot \vec{g} \quad (4)$$

$$\theta_i \cdot \frac{d^2 \vec{\varphi}_i}{dt^2} = \sum_{j=1}^N \vec{M}_{ij} + M_i^r = \sum_{j=1}^N \vec{r}_i \times \vec{F}_{ij} + M_i^r = \vec{M}_i \quad (5)$$

With the mass of the i 'th particle m_i , its moment of inertia θ_i , accelerations $d^2 \vec{x}_i/dt^2$, angular accelerations $d^2 \vec{\varphi}_i/dt^2$ and the external forces \vec{F}_{ij} and moments \vec{M}_{ij} resulting from the contact with particle j are denoted. The contact force acting on both collision-partners can be split in normal and tangential components. The normal force is described with the linear spring dashpot model (Simsek et al., 2009) and acts always in direction of the normal vector \vec{n} (Eq. (6)). The first term represents the elastic repulsion which is proportional to the overlap ξ between the impact partners. The viscous dissipation is proportional to the normal relative velocity v^n . The required contact parameters are the stiffness of a linear spring k^n and the damping coefficient γ^n .

$$\vec{F}^n = \vec{F}_{el}^n + \vec{F}_{diss}^n = (-k^n \xi - \gamma^n v^n) \cdot \vec{n} \quad (6)$$

The tangential force is based on the tangential spring model acting in the direction of the tangential vector \vec{t} . It is the product of the tangential stiffness of a linear spring k^t and the tangential spring elongation ξ^t and is limited by Coulomb's law.

$$\vec{F}^t = - \min\left(\left|k^t \xi^t\right|, \left|\mu_{dyn} \vec{F}^n\right|\right) \cdot \vec{t} \quad (7)$$

The dissipation due to rolling friction is accounted for with the rolling friction vector \vec{M}_i^r always reducing the momentum (Eq. (8)) by opposing the particle's rotation. In this work, the model by Beer and Johnson (1976) is applied where the moment is proportional to the normal force \vec{F}_{ij}^n (Eq. (6)). In Eq. (8) $\vec{\omega}_i$ is the angular velocity vector and μ_r the rolling friction coefficient.

$$\vec{M}_i^r = -\mu_r \left| \vec{F}_{ij}^n \right| \cdot \frac{\vec{\omega}_i}{|\vec{\omega}_i|} \quad \text{with} \quad \omega_i = \frac{d\varphi_i}{dt} \quad (8)$$

The particle's motion is solved by numerical integration of Eqs. (4) and (5). Therefore, the particle forces and momentums for all contacts with other particles or walls are calculated with Eqs. (6) and (7). The single step explicit forward Euler scheme with constant time steps is used because of its simplicity and economy.

2.3.1. The particle phase: particle/fluid phase heat and mass transfer

In case of dense packed beds the heat transfer through the particle contacts, the conduction through the stagnant fluid film near the contact point and the direct radiative heat transfer between particles are the dominant intra-particle heat transfer mechanisms (Yagi and Kunii, 1957) and hence are accounted for in the DEM code. Modeling of contact heat transfer between particles and conduction through the interstitial gas is based on the approach by Vargas and McCarthy (2002). Here the classical elasticity theory of Hertz, (1881) is used to calculate the contact area between two particles. The heat flux induced by these two mechanisms is calculated by

$$q_{con} = \left(\frac{1}{R_c} + \frac{1}{R_g} \right) \cdot (T_{surf,2} - T_{surf,1}) \quad (9)$$

Both modes act in parallel and are governed by the same temperature difference of two particle surfaces. The thermal constriction resistance (direct particle contact) R_c is determined with the contact radius r_c of the circular contact zone

$$R_c = \frac{1}{2 \cdot k_{hm} \cdot r_c} \quad \text{with} \quad r_c = \left(\frac{3 \cdot (1 - \theta_{hm}^2) \cdot |F_n| \cdot r_{hm}}{2 \cdot E_{y,hm}} \right)^{\frac{1}{3}} \quad (10)$$

F_n is the normal force vector acting on the two contacting particles. The first stage DEM simulations of the particle motion in the shaft kiln provide the normal forces for each particle contact. $E_{y,hm}$, r_{hm} , θ_{hm} and k_{hm} are the harmonic mean values of Young's modulus, sphere radius, Poisson's ratio and thermal conductivity of the two particles calculated by the following equation:

$$X_{hm} = 2 \cdot \frac{X_1 \cdot X_2}{X_1 + X_2} \quad \text{with } X \in E_y, r, \theta_p, k \quad (11)$$

The second mode is the heat flux in the stagnant gas zone near the particle contact area with the exposed surface A_g and the average distance l_g

$$R_g = \frac{l_g}{k_g \cdot A_g} \quad \text{with } A_g = 2 \cdot \pi \cdot r^2 - \pi \cdot r_c^2 \quad \text{and } l_g = \frac{r_{hm}^2 \cdot (1 - \frac{\pi}{4})}{r_{hm} - r_c} \quad (12)$$

In addition to the contact heat transfer the direct radiant heat transfer between two particles is described assuming gray body behavior by

$$q_{rad} = \sigma \cdot \varepsilon_m \cdot A_{surf} \cdot (T_{rad,p}^4 - T_{surf}^4) \quad (13)$$

with the emissivity ε_m , depending on the material, temperature and surface condition. In our simulations we used a constant emissivity of $\varepsilon_m=0.93$ (Yagi and Kunii, 1957). For a detailed modeling of radiation exchange between particles the view factors in all spatial directions from each particle have to be determined. This calculation is numerically very expensive, especially for a dense packed bed with high particle numbers. Therefore a "volume of radiation influence" around the observed particle is defined instead of using view factors. This method is based on the assumption that all particles within this radiation volume are in exchange with the observed particle. In the simulation the radiation volume is defined as a sphere around the absorbing particle with the radius ($r_{rad,area} = 1.5 \cdot d_p$). Here, d_p is the diameter of the absorbing particle. By this approach an average temperature $T_{rad,p}$ of the surrounding can be determined and thus a net heat flow for each particle can be calculated with Eq. (14). The surrounding temperature is defined as the sum over all emitted heat flows of j particles inside the radiation volume weighted by the surface and emissivity of each particle. The validity of the simplified particle-particle radiation model developed was verified with experimental data (Yagi and Kunii, 1957) and numerical simulations.

$$T_{rad,p}^4 = \frac{\sum_j \sigma \cdot A_{surf,j} \cdot \varepsilon_j \cdot T_{surf,j}^4}{\sum_j \sigma \cdot A_{surf,j} \cdot \varepsilon_j} \quad (14)$$

The interphase heat transfer by convection for a particle is given by

$$q_{conv} = h_p \cdot A_{surf} \cdot (T_f - T_{surf}) \quad (15)$$

The fluid temperature T_f and the convection coefficient h_p are assumed to be spatially constant over a particle's surface. The convection coefficient h_p is calculated with the established Nusselt-correlations of Gnielinski (Gnielinski, 1978) for single spherical particles. It covers Reynolds numbers up to 10^5 and Prandtl numbers from 0.7 to 70,000 (Aschenbach, 1995; Gnielinski, 2006)

$$Nu_p = 2 + \sqrt{Nu_{lam}^2 + Nu_{turb}^2} \quad (16)$$

$$Nu_{lam} = 0.664 \cdot Re^{1/2} \cdot Pr^{1/3} \quad (17)$$

$$Nu_{turb} = \frac{0.037 \cdot Re^{0.8} \cdot Pr}{1 + 2.443 \cdot Re^{-0.1} \cdot (Pr^{2/3} - 1)} \quad (18)$$

Gnielinski applied a correction factor f_e accounting for increased heat transfer of packed beds which is characterized by the porosity ϕ . This correction factor is valid in a range $0.26 < \phi < 1$.

$$Nu = f_e \cdot Nu_p \quad \text{with } f_e = 1 + 1.5 \cdot (1 - \phi) \quad (19)$$

The Nusselt number is defined as $Nu = h_p \cdot L_c/k_f$, Reynolds number as $Re = v_{phys,f} \cdot L_c/\nu_f$ and the Prandtl number as $Pr = \nu_f/\alpha_f$. Here $v_{phys,f}$, k_f , ν_f and α_f are the physical velocity, the thermal conductivity, the kinematic viscosity and the thermal diffusivity of the fluid, respectively. These temperature dependent gas properties are provided by the CFD code. As characteristic length scale L_c the particle diameter d_p must be used. Analogously, the Sherwood number of each species i ($Sh_i = \beta_i \cdot L_c/D_i$) is calculated from the Schmidt ($Sc_i = \nu_f/D_i$) and Reynolds numbers. The interphase mass transfer of the species i is then computed from the mass transfer coefficient $\beta_{i,eff}$ and the concentration gradient $\Delta Y_i = Y_{i,f} - Y_{i,surf}$ (see Section 2.3.2).

2.3.2. The particle phase: inner particle heat and mass transfer

Beside the heat and mass transfer between gas and solid phase the transport inside each particle is considered. The description of inner particle heat transfer is important because strong inner particle temperatures gradients occur during the heat up and cooling stage due to the larger size of typical limestone particles (about several centimeters). In addition inner particle heat sinks by the endothermic calcination reaction strengthen the forming of temperature gradients and have to be taken into account. The reaction front moving through the particle core creates a porous outer shell of CaO characterized by a low thermal conductivity. Thus a "hot" shell of CaO and a "cold" core of CaCO₃ arise as a result of the reaction process. Particularly during the calcination process, the description of inner particle mass transfer is also important. The CO₂ bound in the limestone and released by the calcination reaction has to be transported through the voids of the porous limestone particle to the surrounding gas phase. To account for inner particle heat and mass transport a one-dimensional model for a porous spherical limestone particle has been implemented. Certain assumptions and simplifications are required (Takkinen, 2012):

- The boundary conditions and initial conditions are symmetrically and spatially constant, thus, 1-D analysis is applied.
- The heat and mass sources and the transport within the particle are one-dimensional.
- Changes in shape and size (diameter) of the particle are not considered (fragmentation and attrition do not occur).

The set of non-linear diffusional equations listed below is solved by discretization of the particle along the radius using equally spaced nodes. Thus, the volume of the spherical particle is subdivided in multiple shells. The integral form of the heat conservation equation is written as follows:

$$\frac{d}{dt} \int_V \rho_{s,eff} c_{p,s,eff} T dV = - \oint_A (k_{s,eff} \nabla T) \cdot \vec{n} dA + \int_V S_R dV \quad (20)$$

S_R is the heat of decomposition reaction induced in this volume element (Eq. (51)). The macro-kinetic model describing the rates of the decomposition reaction is presented in Section 2.3.3. The effective

values $\rho_{s,eff}$, $c_{p,s,eff}$ and $k_{s,eff}$ of each volume element are calculated using the data from Table 2 and the following Eqs. (21)–(23)

$$\frac{1}{\rho_{s,eff}} = \frac{Y_{CaO}}{\rho_{t,CaO} \cdot (1 - \epsilon_{s,CaO})} + \frac{Y_{CaCO_3}}{\rho_{t,CaCO_3} \cdot (1 - \epsilon_{s,CaCO_3})} \quad (21)$$

$$c_{p,s,eff} = Y_{CaO} \cdot c_{p,s,CaO} + Y_{CaCO_3} \cdot c_{p,s,CaCO_3} \quad (22)$$

$$k_{s,eff} = Y_{CaO} \cdot k_{s,CaO} + Y_{CaCO_3} \cdot k_{s,CaCO_3} \quad (23)$$

Boundary conditions in the particle's center and at the surface are

$$r = 0; k_s \frac{\partial T}{\partial r} = 0 \quad (24)$$

$$r = R_p; \int_{A_{surf}} (k_{s,eff} \nabla T) \cdot \vec{n} dA = h_p \cdot A_{surf} \cdot (T_f - T(r = R_p)) + S_R(r = R_p) + q_{con} + q_{rad} \quad (25)$$

The heat transfer through particle contacts and the conduction through the fluid film near the contact points are represented by q_{con} and the direct radiant heat transfer between particles by q_{rad} . The variables $T(r = R_p)$ and $S_R(r = R_p)$ represent the temperature and heat source in the outermost shell element n ($n = \infty (r = R_p)$). The integral form of the mass conservation equation is given by

$$\frac{d}{dt} \int_V \epsilon_s \rho_g dV = - \oint_A (\epsilon_s \rho_g \vec{v}_g) \cdot \vec{n} dA + \int_V S_R dV = 0 \quad (26)$$

S_R is the mass source released in this volume element due to the calcination reaction. The conservation of mass and momentum is used for solving gas velocity and pressure in the porous particle. Darcy's law for porous media is applied to the momentum equation, giving the following velocity and pressure relation (Takkinen, 2012):

$$\vec{v}_g = - \frac{\kappa_s}{\mu_g} \nabla P_g \quad (27)$$

The effect of the porous structure changes on the inner particle pressure drop is assumed to be negligible. Thus, a constant value for the limestone permeability κ_s is used. The permeabilities of limestone may differ significantly (Lech, 2007) and can change during the calcination process. Typical values can be found in the range between 10^{-13} and 10^{-16} m². The gas mixture's dynamic viscosity is computed as a mass fraction average of the pure species dynamic viscosities. The conservation equation of a chemical species i is written as follows:

$$\frac{d}{dt} \int_V \epsilon_s \rho_g Y_i dV = - \oint_A (\epsilon_s \rho_g \vec{v}_g Y_i - \epsilon_s \rho_g D_{i,eff} \nabla Y_i) \cdot \vec{n} dA + \int_V S_{i,R} dV \quad (28)$$

$S_{i,R}$ is the net rate of production of species i by chemical reaction and therefore only relevant for CO₂ due to the calcination reaction (see Eq. (49) in Section 2.3.3). The first term on the right hand side accounts for advection and the second for diffusion. The advective mass transport is caused by inner particle pressure gradients. These pressure gradients are related to the limestone decomposition, because the released CO₂ increases the pressure in the voids close to the reaction front. Fluxes of solid species in the particle are assumed to be zero. Three gas species (CO₂, O₂ and N₂) and two solids (CaO and CaCO₃) are considered. The local void fraction of the solid structure ϵ_s is assumed to remain constant at the value for CaO and does not change during the calcination

process. Boundary conditions at the particle's center and at its surface are

$$r = 0; \epsilon_s \cdot \rho_g \cdot \frac{\partial Y_i}{\partial r} = 0; \epsilon_s \cdot \frac{\partial \rho_g}{\partial r} \quad (29)$$

$$r = R_p; \phi \cdot \rho_g \cdot \frac{\partial Y_i}{\partial r} = \beta_i \cdot \rho_f \cdot (Y_{i,f} - Y_i(r = R)) + S_i(r = R) \quad (30)$$

Here the index f represents the properties of the surrounding fluid phase described with the CFD-Code. The surface boundary condition in this form (Eq. (30)) with the diffusional mass transfer coefficient β_i calculated by the Sherwood theory (Section 2.3.1) only considers mass transfer to the surrounding fluid phase via diffusion neglecting the effect of advection. Beside the diffusional transport the inner-particle advection leads to a movement of chemicals species by fluid flowing away from the particle surface. This transport phenomenon, known as Stefan flow (Zogg, 1983), is distinct from diffusion and independent from concentration gradients.

In the presented DEM/CFD coupling method the mass transport between the solid (DEM) and fluid (CFD) phase is realized by a diffusive species source term on the CFD side. This source term ($S_{i,CFD}$) in the species conservation equation is linearized with respect to the species concentration $Y_{i,CFD}$ in the CFD cell

$$S_{i,CFD} = \underbrace{B_{const} Y_{i,p}(r = R)}_{\text{constant}} - \underbrace{B_{const}}_{\text{linearized}} \cdot Y_{i,CFD} \quad (31)$$

with

$$B_{const} = \beta_{i,eff} \cdot A_{surf} \cdot \frac{\rho_{f,CFD}}{V_{c,CFD}} \quad (32)$$

This linearization method only describes a diffusive interphase mass transfer but strongly increases numerical stability and accuracy for the steady fluid flow. However, in most cases the advection term (Stefan flow) increases the total mass flow rate further. The transferred mass flow rate via diffusion of the species i is calculated as follows:

$$\dot{m}_{i,surf,diff} = \beta_i \cdot \rho_f \cdot A_{surf} (Y_{i,f} - Y_i(r = R)) \quad (33)$$

To consider the second mass transfer mechanism, the mass flow rate at the particle surface induced by advection is calculated. Therefore it is assumed, that the species advection mass flow is equal to the mass flow in the outermost volume element n ($n = \infty (r = R)$). The total transport rate of the species is then given by a summation of the Stefan flow and the diffusive contributions.

$$\dot{m}_{i,surf,Stefan} = \epsilon(n) \cdot \rho_g(n) \cdot A_{surf} \cdot v(n) \cdot Y_i(n) \quad (34)$$

Regarding these two terms, an effective mass transfer $\beta_{i,eff}$ coefficient is determined and is used in Eq. (30) replacing β_i .

$$\beta_{i,eff} = \beta_i \cdot \frac{\dot{m}_{i,surf,diff} + \dot{m}_{i,surf,Stefan}}{\dot{m}_{i,surf,diff}} \quad (35)$$

With this simplified approach the increased mass transfer by advection is considered in the particle surface linearized diffusive boundary condition. Furthermore the gas concentration gradient ($Y_{i,f} - Y_i(r = R)$) which directly influences the concentration profile in the particle remains unaffected.

The effective diffusion coefficient of a species i in a porous medium j is defined as

$$D_{i,eff,j} = \kappa_{Kn,j} \cdot \left(\frac{1}{D_{i,K,j}} + \frac{1}{D_i} \right)^{-1} \quad (36)$$

In order to obtain effective diffusion coefficients, the combined diffusion coefficients are multiplied by the permeability $\kappa_{Kn,j}$. The permeability is the ratio between the materials internal porosity and tortuosity (Satterfield and Sherwood, 1963) and calculated from:

$$\kappa_{Kn,j} = \frac{\epsilon_{s,j}}{\tau} \quad (37)$$

The binary diffusion coefficients D_i are estimated by the Fuller, Schuettler and Giddings' equation (FSG) for the 3 pairs out of 3 gas species (Fuller et al., 1966). The Knudsen diffusion coefficients of a species i through the material component j (CaO or CaCO_3) is given by Eq. (38).

$$D_{i,K,j} = \frac{2}{3} r_{pore,j} \sqrt{\frac{8 R T}{\pi M_i}} \quad (38)$$

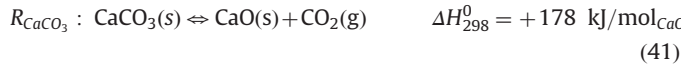
$$r_{pore,j} = 2 \frac{\epsilon_{s,j}}{S_{e,j}} \quad (39)$$

The void fraction ϵ_s and specific surface area $S_{e,j}$ of the two compounds CaO and CaCO_3 are presented in Table 2. Finally the effective diffusion coefficient of a species i in the porous limestone is defined as the series connection from the two components weighted by mass fractions

$$D_{i,eff} = Y_{\text{CaO}} \cdot D_{i,eff,\text{CaO}} + Y_{\text{CaCO}_3} \cdot D_{i,eff,\text{CaCO}_3} \quad (40)$$

2.3.3. The particle phase: reaction model for calcination

The main reaction for the endothermic decomposition of CaCO_3 is the calcination or dissociation of CO_2



The spatially distribution of the calcium carbonate decomposition rates in the particle is controlled by the local solid temperature and the CO_2 concentration. The local CaCO_3 mass source of one volume element of the discretized particle is calculated with

$$\frac{\partial m_{\text{CaCO}_3}}{\partial t} = -A_{rf} \cdot M_{\text{CaCO}_3} \cdot k_{r,\text{CaCO}_3} \cdot (c_{\text{CO}_2} - c_{\text{CO}_2,\infty}) \quad (42)$$

With the relation between the mass source of the three participating species

$$\frac{\partial m_{\text{CaCO}_3}(s)}{\partial t} = \frac{\partial m_{\text{CaO}}(s)}{\partial t} + \frac{\partial m_{\text{CO}_2}(g)}{\partial t} \quad (43)$$

The surface of the active reaction front is represented by A_{rf} which is the mean surface of the corresponding volume element. In cases of spherical particles the surface of the volume element i is calculated with

$$A_{rf,i} = 4 \pi \left(\frac{r_{p,i} + r_{p,i-1}}{2} \right)^2 \quad (44)$$

The driving force of the reaction is the local concentration gradient between the CO_2 concentration in the voids of the porous limestone and the equilibrium concentration. If the CO_2 concentration raises above the equilibrium concentration the reaction

(Eq. (42)) is reversed and CaCO_3 is formed. The equilibrium concentration is calculated by Eq. (45) and strongly depends on the local solid temperature.

$$c_{\text{CO}_2,\infty} = \frac{p_{\text{CO}_2,\infty}}{R \cdot T_s} \quad (45)$$

The CO_2 equilibrium pressure $p_{\text{CO}_2,\infty}$ [Pa] is calculated with the solid temperature T_s [K] according to Hills (1968) using the following expression:

$$p_{\text{CO}_2,\infty} = 101,325 \cdot \exp \left(17.74 - 0.00108 T_s + 0.332 \ln(T_s) - \frac{22,020}{T_s} \right); T_s [\text{K}] \quad (46)$$

The chemical rate constant k_{r,CaCO_3} is calculated according to Vonderbank et al., (1993)

$$k_{r,\text{CaCO}_3} = A k_{r,\text{CaCO}_3} \cdot T_s \cdot \exp \left(-\frac{4026}{T_s} \right) \cdot Y_{T,C}; \quad A k_{r,\text{CaCO}_3} = 1.0 \cdot 10^{-4} \quad (47)$$

Vonderbank established the temperature dependent correction factor $Y_{T,C}$ based on measurements (Chugtai and Michelfelder, 1983)

$$Y_{T,C} = \frac{480}{T_s - 958}; \quad T_s [\text{K}] > 1150 \text{ K} \\ Y_{T,C} = 2.5; \quad T_s [\text{K}] \leq 1150 \text{ K} \quad (48)$$

The net rate of production of CO_2 by calcination $S_{\text{CO}_2,R}$ is acting as a mass source in Eqs. (28) and (30) and is calculated with Eq. (49). The net rate of the other two species (O_2 and N_2) is always zero because they do not act as reactants

$$S_{\text{CO}_2,R} = \frac{\partial m_{\text{CaCO}_3}(s)}{\partial t} \cdot \frac{M_{\text{CO}_2}}{M_{\text{CaCO}_3}} \cdot \frac{1}{V_n} \quad (49)$$

The calcination heat source applied in the energy transport equation (Eqs. (20) and (25)) depends on the reaction temperature and the heat capacities of the participating species (see Table 2)

$$\Delta H_{T_s}^0 = \Delta H_{298}^0 + \int_{T=298}^{T_s} (c_{p,\text{CO}_2} \cdot M_{\text{CO}_2} + c_{p,\text{CaO}} \cdot M_{\text{CaO}} - c_{p,\text{CaCO}_3} \cdot M_{\text{CaCO}_3}) dT \quad (50)$$

$$S_R = \Delta H_{T_s}^0 \cdot \frac{S_{\text{CO}_2,R}}{M_{\text{CO}_2}} \quad (51)$$

3. Results of laboratory scale calcium carbonate decomposition

Hills (1968) performed thermo-gravimetric analyses of the decomposition of single spheres of pure calcium carbonate. The weight loss of the samples was measured in a high temperature tube furnace passed by air or an air/ CO_2 mixture. The stream temperature was kept constant. A thin wire thermocouple was placed in the particles core and the time-temperature curve of the particle core was determined. The sintered samples of pure calcium carbonate had an outer diameter of approximately 10 mm.

Each run was started with the sample at thermal equilibrium. Therefore pure CO_2 was used as gas flow during the heat-up phase. Hence the voids in the sample were saturated with CO_2 and as described by Eq. (42), the high CO_2 concentration suppresses the decomposition at temperatures below 900 °C. After the sample has reached the preset gas temperature, the flow was abruptly changed to the desired air/ CO_2 mixture with the same gas phase

temperature. The CO₂ contained in the sample diffuses into the gas phase and the decomposition sets in.

Simulations of the laboratory scale apparatus are compared with the experimental results as a verification of the proposed model. The particle properties used and the boundary conditions are listed in Table 2. They are in the typical range for limestone material (Do and Specht, 2011; Cheng and Specht, 2006; Moropoulou et al., 2001). Note that the particle properties proposed in the literature are subject to large variations due to different origins of the limestone.

We assumed a constant heat transfer coefficient at the particle surface and particle related Reynolds numbers based on calculations of Hills (1968). The diffusional mass transfer coefficient β_i is determined from the Nusselt theory (see Section 2.3.1). The gas phase properties acting as boundary conditions at the particle surface were set constant during the simulation according to the set of parameters for each simulation run (see Table 1).

In Figs. 2 and 3 the simulations results are compared with the experimental data by plotting the conversion progress of the sample (calcination degree c^*) versus time. The degree of calcination is calculated as:

$$c^* = \frac{m_0 - m(t)}{m_0 - m_\infty} \quad (52)$$

The good agreement with the measurements confirms that the model approach is appropriate for the simulation of the conversion of limestone particles. It can reproduce the effect of higher CO₂ concentrations in the gas phase reducing the decomposition rate (Fig. 3) as well as the dependency between the decomposition rate and the gas temperature. Further effects and dependencies which could be reproduced successfully are described in (Bluhm-Drenhaus et al., 2010) in more detail.

Table 1
Gas phase conditions for the experimental runs (Hills, 1968).

Run	26	28	30	35	41	45	52
Temperature [°C]	877	876	874	877	902	829	720
CO ₂ mole fraction [dimensionless]	0	0.106	0.154	0.323	0	0	0

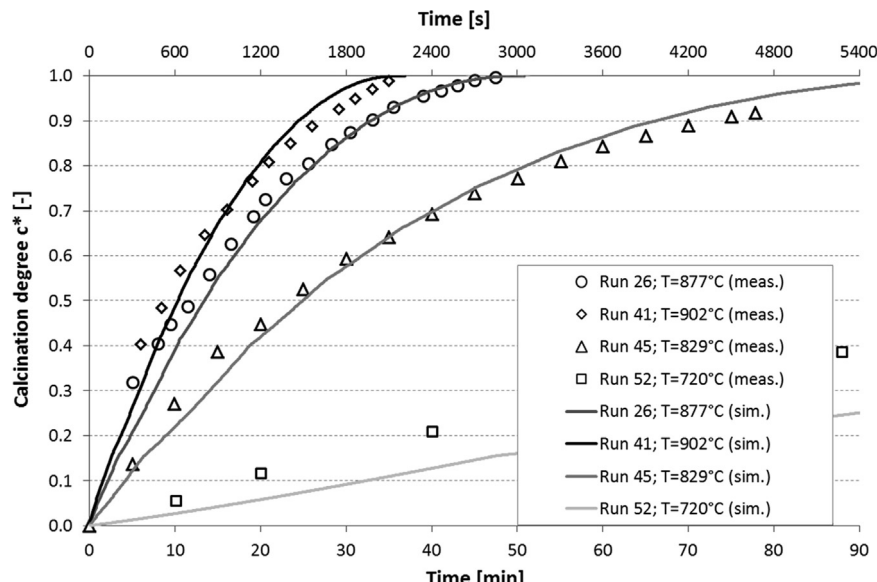


Fig. 2. Variation of the gas temperature – Comparison between simulation results and experimental data (Hills, 1968), measured data shown as symbols, simulation data as lines (single particle study).

Fig. 4 compares the simulated temperature profile at the particle core with the measurements. Starting at gas temperature (thermal equilibrium) the core temperature shows the characteristic steep decrease due to the fast onset of the endothermic calcination reaction. The minimum temperature is reached when the energy consumed by the reaction equals the heat flux to the reaction front due to conduction. With the growth of the outer calcined CaO shell the mass transfer of the released CO₂ at the reaction front to the surrounding gas phase becomes the rate determining step. Thus the particle core temperature converges slowly to the gas phase temperature. This specific development of the core temperature is reproduced by the current model approach with high accuracy and temperature deviations below 20 °C.

These results underline the good agreement of the model for limestone with greater diameters around 1 cm. However in the lime industry pieces of several centimeters are usually converted (Cheng and Specht, 2006). Therefore the crushed limestone is screened to remove smaller particles in order to reduce the pressure loss in the system. To verify that the model approach is appropriate for the simulation of limestone particles larger than 1 cm, we used experimental data from Specht (Do and Specht, 2011; Cheng and Specht, 2006). The experimental apparatus and the measurement procedure is comparable to that of Hills and described in more detail in Do and Specht (2011), Cheng and Specht (2006). The measurements were performed using spheres and cylinders with diameters from 20 to 47 mm. The length/diameter ratios of the cylinders ranged from 5 to 12, so that they could be regarded as infinitely long and treated as one-dimensional (Cheng and Specht, 2006). For each run the core temperature and the degree of conversion was recorded over time. These results were used to evaluate the reaction rate coefficients, the pore diffusivity and the thermal conductivity of the lime layer using an analytical solution based on the shrinking core model.

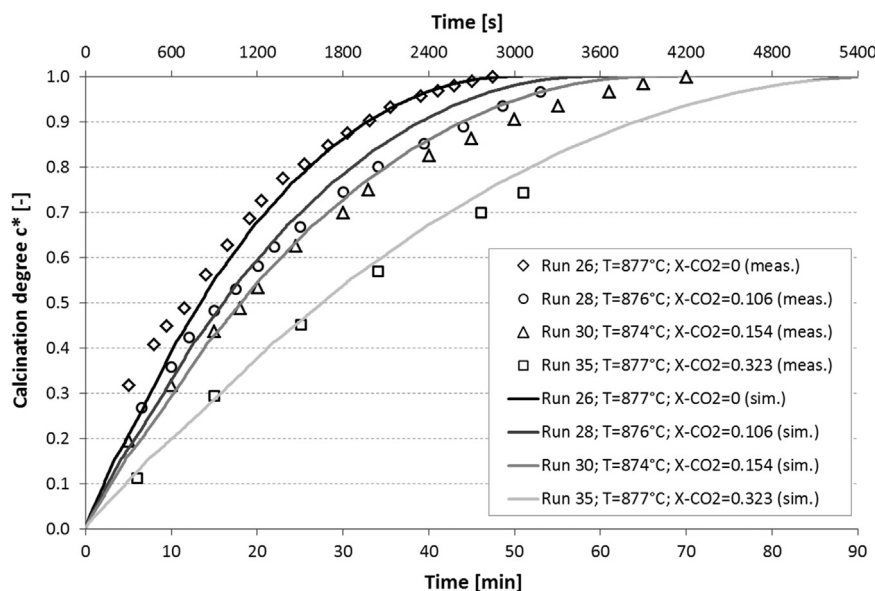


Fig. 3. Variation of the CO₂ concentration - Comparison between simulation results and experimental data (Hills, 1968), measured data shown as symbols, simulation data as lines (single particle study).

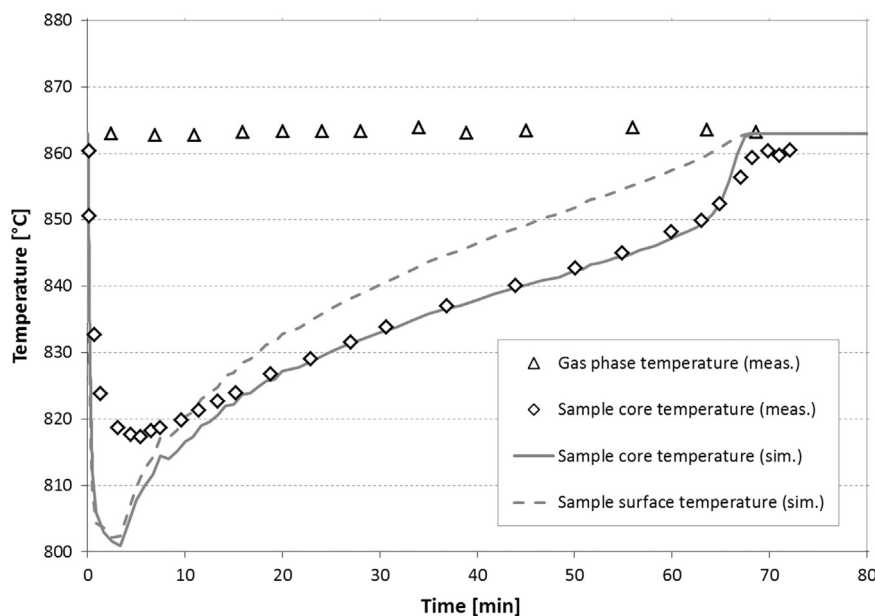


Fig. 4. Simulated core and surface temperature of a 10 mm sample during the decomposition in a furnace held at 863 °C and swept with pure air, measurement data shown as symbols (Hills, 1968), simulation data as lines (single particle study).

Table 2
Particle properties and simulation boundary conditions (Hills, 1968).

Symbol	Unit	Value	Symbol	Unit	CaCO ₃	CaO
d_p	[mm]	10	$\rho_{s,j}$	[kg/m ³]	2812.05	3310.00
Re_p	[dimensionless]	2.4	$c_{p,s,j}$	[J/kg/K]	836.8	753.1
h	[W/m ² /K]	90.0	$k_{s,j}$	[W/m/K]	2.26	0.07
κ_s	[m ²]	$7 \cdot 10^{-15}$	$\varepsilon_{s,j}$	[dimensionless]	0.040	0.543
τ	[dimensionless]	1.41	$S_{e,j}$	[m ² /kg]	16,000	7000

Limestone of 10 different origins was examined showing that the material properties vary up to factors of 10.

For the model verification we used experimental data from cylindrical specimens with two different diameters (25 mm (Cheng and Specht, 2006) and 47 mm (Do and Specht, 2011))

and two different limestone origins named "SPGe1" and "SPGe3" (Do and Specht, 2011). In order to account for two different limestone origins in our simulations we adjusted the particle properties and boundary conditions based on the results from Do and Specht. The values used are listed in Table 3. The unlisted

values were taken from the simulations of Hills and can be found in Table 2.

For three simulations Fig. 5 compares the simulated temporal temperature profile of the particle core with the corresponding measurements. The experiments were not started at thermal equilibrium resulting in a steep temperature rise of the specimens in the first ten minutes. The core temperature rises up to the point where decomposition sets in and remains at this temperature for almost the complete decomposition process. These two effects could be sufficiently reproduced in the simulations. With about 830 °C, the simulated equilibrium temperature is about 50 °C lower than the measured value. This is primarily due to the kinetic reaction model presented in Section 2.3.3. This model leads to higher reaction rates for temperatures around 830 °C which corresponds well with the measurements from Hills, but results in minor deviations for the limestone samples tested by Specht et al.

Subsequent to the interval characterized by the constant equilibrium temperature another temperature rise up to the gas temperature follows. This second steep rise sets in when the calcination front reaches the particle core and the decomposition is almost complete. The higher temperature gradients in the simulation could be attributed to a higher thermal conductivity in the CaO shell or lower CO₂ concentrations in the voids near the

particle core resulting in higher reaction rates. The third run (SPGe3; $d=47$ mm), which is plotted on the upper time scale, experiences the largest deviations. The limestone origin for this experimental run was not labeled, so we assumed that the material properties are similar to those from SPGe3.

Fig. 6 compares the simulation with the measurements by plotting the calcination degree of the samples versus time. For both factors, the particle diameter and the limestone origin, there is a good agreement between the measured and simulated decomposition process. These results confirm the suitability of the new model approach to describe the decomposition behavior of particles in a wide range of diameter, temperature and gas concentration. Furthermore it is capable to consider the material properties of different limestone origins and their influence on decomposition.

4. Simulation of a lime shaft kiln

In an industrial lime shaft kiln, a major difficulty is to ensure an uniform radial temperature distribution in the calcination zone. The fuel gas is injected via burners at the kiln wall and in vicinity to the calcination zone and usually a radial temperature gradient develops with high temperatures close to the wall. Thus, there is a risk of an incomplete decomposition of particles in the kiln center due to lower temperatures and a potential product quality decrease near the wall due to sintering (high calcination temperatures).

For the numerical investigation a simplified vertical lime shaft kiln is selected as shown in Fig. 7. The kiln height is 9.5 m with a diameter of 1.5 m. The computational domain is reduced to a quarter-model by periodic boundary conditions. The hexahedral mesh for the CFD-simulation consists of about 120,000 cells and the DEM simulation considers about 25,000 particles. The burner level is 3.8 m above the limestone discharge. Note that in the current work a simplified approach for the representation of the burner has been selected. The fuel gas is injected through the complete annular section, thus an arrangement of burner lances is not considered. This approach was selected to simplify the structure of the CFD-mesh used. Furthermore we wanted to ensure

Table 3
Particle properties and simulation boundary conditions (Do and Specht, 2011).

Symbol	Unit	Value	Symbol	Unit	Value
d_p	[mm]	25; 47	Re_p	[–]	5.0
h_{zy}/d_p	[dimensionless]	10.0	h	[W/m ² /K]	150.0
τ	[dimensionless]	1.41			
Symbol	Unit	SPGe1	SPGe3		
		CaCO ₃	CaO	CaCO ₃	CaO
$k_{s,j}$	[W/m/K]	2,260	0.070	2,009	0.062
$S_{e,j}$	[m ² /kg]	16,000	7000	10,870	4755
κ_s	[m ²]	$7.0 \cdot 10^{-15}$		$10.3 \cdot 10^{-15}$	
$AK_{r,CaCO_3}$	[m/s]	$1.00 \cdot 10^{-4}$		$0.82 \cdot 10^{-4}$	

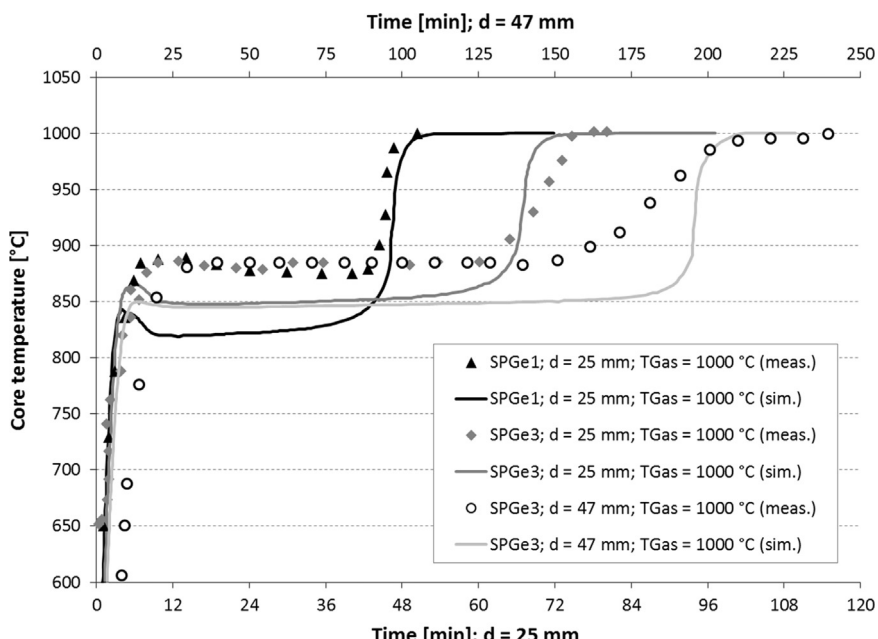


Fig. 5. Simulated and measured core temperatures for the different samples during the decomposition in a furnace held at 1000 °C and swept with pure air, measurement data shown as symbols (Do and Specht, 2011; Cheng and Specht, 2006), simulation data as lines (single particle study).

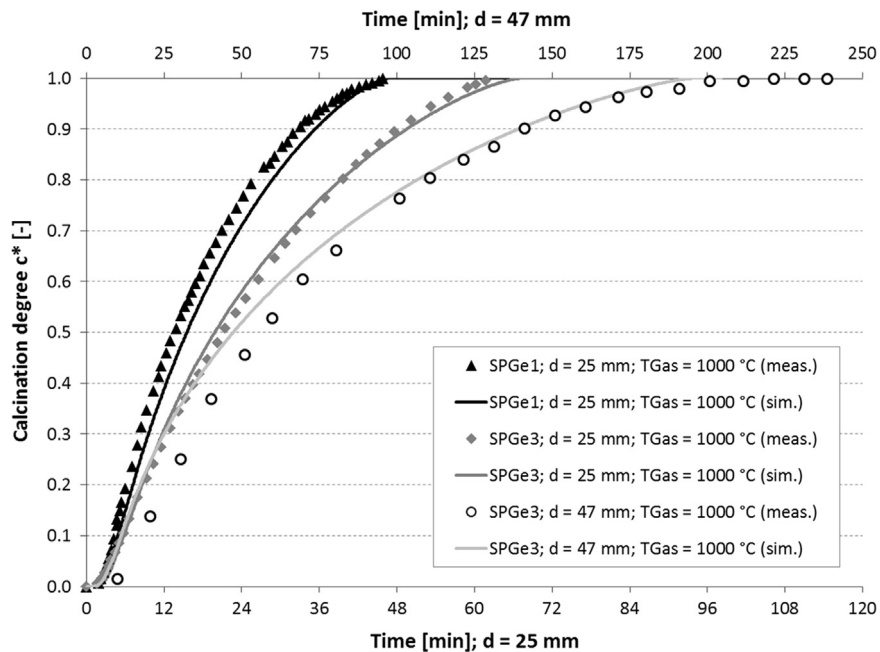


Fig. 6. Simulated and measured calcination degree for the different samples during the decomposition in a furnace held at 1000 °C and swept with pure air, measurement data shown as symbols (Do and Specht, 2011; Cheng and Specht, 2006), simulation data as lines (single particle study).

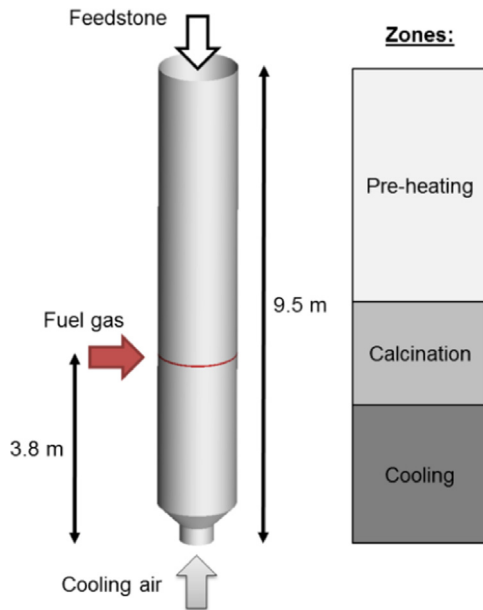


Fig. 7. Geometry and size of the simulated vertical shaft kiln with input streams.

that the effect of temperature gradients in the fixed bed is confined to the radial direction and does not depend on the arrangement of the burner lances. However, no fundamental obstacle exists to include burner lances in the simulation and the method can be also applied to other kiln types featuring more complex flow pattern. The stoichiometric factor of the air/methane mixture injected via the burner section is 0.7. This stoichiometry was chosen in order to increase the combustion temperature by using the pre-heated cooling air as secondary combustion air.

All model parameters and boundary conditions used for the kiln simulation are summarized in Table 4. The material properties of the limestone and quicklime are taken from Table 2. The coupled DEM/CFD domain is the limestone bed with porosity

distribution determined from the previous DEM simulations of the particle movement in the kiln (see Fig. 11).

4.1. Results

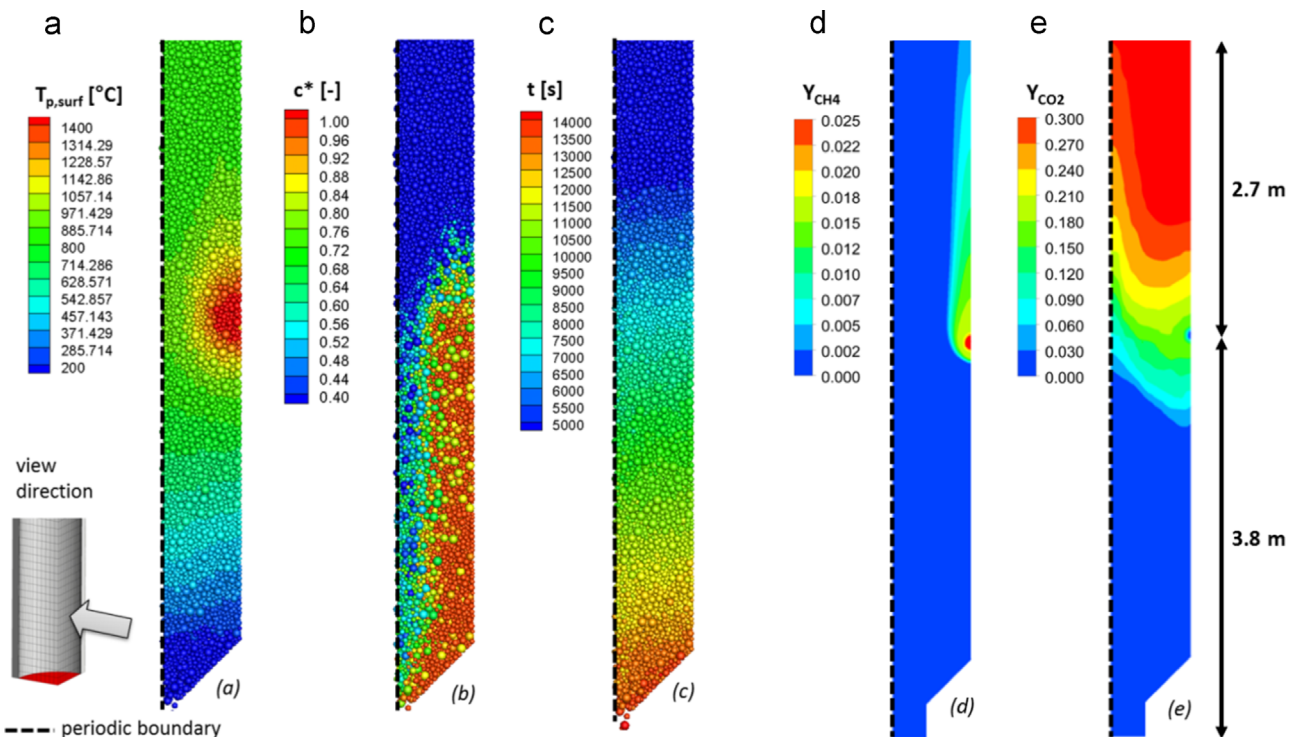
In Fig. 8 the fluid and particle data of the 6.5 m kiln height are plotted (Run A). The sketch on the bottom left illustrates the view direction. From left to right the first image (a) shows the particle surface temperatures. A strong radial temperature profile exists at the burner level height (3.8 m) with high temperatures near the inner kiln wall and low temperatures at the center. The fourth image (d) plots the mass fraction of methane in the fluid phase. The majority of methane reacts near the kiln wall and due to the high resistance of the particle bed to the gas flow (Eq. (1)), the fuel cannot advance towards the center. Furthermore the incomplete combustion ($\lambda=0.7$) induces a methane plume close to the wall. This effect is enhanced by the fuel mass flow and high temperatures near the burner section, forcing the cooling air (pre-heated secondary combustion air) away from the wall. These results point out a main challenge for the design of lime shaft kilns, which is to achieve complete combustion and flat radial temperature profiles in the calcination zone.

The second image (b) plots the degree of calcination of each individual particle pointing out the second main challenge. The kiln operates with a poor efficiency in the center due to lower gas temperatures. Thus, the conversion rates near the kiln wall or combustion zone (see image (d)) are about 1.5 times higher. Furthermore, the broad particle size distribution in the limestone bed leads to significant differences in the calcination degrees achieved (see Fig. 9). The third image (c) shows the particle residence times in steady state operation. The mean residence time of approximately 4 h is met by the majority of the particles. The particles near the wall have marginally longer residence times caused by wall friction. But the radial residence time distribution is almost even, thus a core flow does not exist. A benefit of the developed one-dimensional particle model is shown in the last plot (e). Here a CO₂ plume moves towards the cooling zone due to the release of the CO₂ bound in the particles voids is limited by diffusion, advection and the CO₂ concentration in the fluid phase.

Table 4

Model parameters and boundary conditions (values valid for the complete kiln – no 1/4 model).

Conditions	Unit	Value	Fluid phase models:	Unit	Value
Kiln height	[m]	9.5	Density	[kg/m ³]	"ideal gas"
Kiln diameter	[m]	1.5	Dyn. viscosity mixture	[kg/m/s]	"mixing law"
Bed height	[m]	8	Specific heat mixture	[J/kg/K]	"mixing law"
Discharge diameter	[m]	0.65	Solid phase parameters:	Unit	Value
Angle of cone	[°]	45	Material properties		See Table 2
Inlet temperature (CaCO ₃ , cooling air & fuel gas)	[°C]	20	Particle size distribution (evenly mass distributed)	[mm]	40, 50, 60, 70, 80, 90
Flow rate cooling air	[Nm ³ /h]	1900	Averaged bed porosity	[dimensionless]	0.35
Flow rate CH ₄	[Nm ³ /h]	408	Feed flow (pure CaCO ₃)	[tpd]	145.6
Flow rate combustion air	[Nm ³ /h]	2720	Particle residence time	[h]	4
Stoichiometric factor λ	[dimensionless]	0.7			
Thermal input	[kW]	3940			
Collision parameter (DEM) – Sphere on sphere and sphere on wall					
Coefficient of restitution e^n	[dimensionless]	0.05			
Stiffness of a normal linear spring k^n	[kg/s ²]	$1.0 \cdot 10^5$			
Damping coefficient γ^n	[kg/s]	12.5			
Stiffness of a tangential linear spring k^t	[kg/s ²]	$8.6 \cdot 10^4$			

**Fig. 8.** Particle surface temperatures (a), calcination degrees (b) and residence times (c), mass fraction of CH₄ (d) and CO₂ (e) in the fluid phase (Run A).

This effect cannot be described by a shrinking core model which does not consider the accumulation of CO₂ in the voids of the porous particle.

The two diagrams in Fig. 9 present mass averaged data at the outlet of the kiln for the different particle size classes. For this purpose a sample of 5000 particles was analyzed in steady state operation. The distribution of the calcination degree shown in the left diagram underlines the effect of a broad size distribution.

Most of the smaller particles are completely calcined, whereas larger particles show a lesser degree of conversion. Larger particles require considerably longer residence times in the calcination zone due to the effect of thermal resistance in the CaO shell, which inhibits conduction of heat towards the reaction front. This effect is hard to describe with continuum models and a simplified treatment of the polydisperse bed as a domain with an average particle diameter would not be justified under these conditions. This is one advantage of the coupled DEM/CFD method describing

each individual particle in the bed. Another outcome which can be traced back to the broad size distribution is the particle temperature distribution at the kiln discharge (right diagram). The mean outlet temperatures of larger particles are higher compared to smaller particles. In the same way inner particle temperature differences increase with the particle size. The average temperature difference between the particle core and surface for the largest diameter class (90 mm) is about three times greater compared to the smallest class (40 mm). These inner particle temperature gradients cannot be described with the shrinking core approach not taking into account inner particle heat transfer (see Section 2.3.2).

The model approach for porous spherical limestone particles presented in Section 2.3.2 considers the inner particle mass transport via diffusion and advection. Underlining the importance of these two mass transfer mechanisms in lime shaft kilns an additional simulation (Run B) was carried out. In Run B the mass

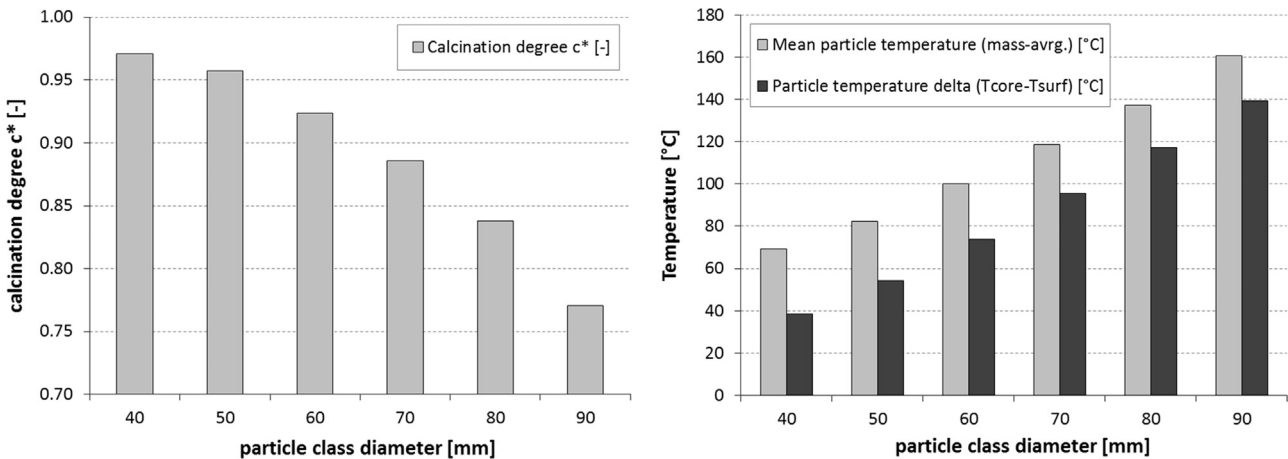


Fig. 9. Mass averaged particle calcination degree, mean particle temperature and inner particle temperature difference ($T_{core}-T_{surf}$) at the outlet separated according to particle size (Run A; sample $N=5000$).

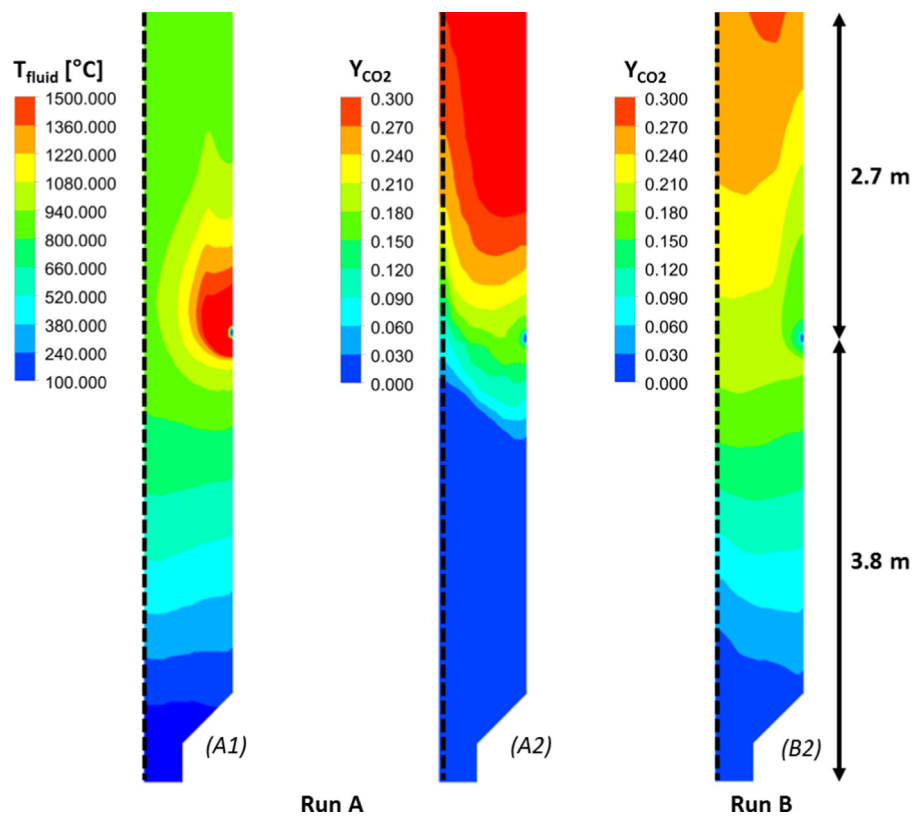


Fig. 10. Fluid temperature for Run A (A1) and CO_2 mass fraction in the fluid phase for Run A (A2) and Run B (B2).

transport via advection is completely disabled and only diffusional mass transport is considered.

Fig. 10 compares the results of Run A (left) with those of Run B (right). In Run B the inner particle mass transport via advection is deactivated resulting in distinctly lower release rates of CO_2 . The particles need higher residence times to release the complete CO_2 leading to high CO_2 concentration in the cooling zone (B2). This effect increases with higher particle diameters, short residence times in the calcination zone and a high fluid temperature. However, this simulation result does not correspond with known kiln behavior. A high CO_2 concentration in the cooling zone, which is characterized by low particle temperatures, would result in a reverse reaction with a formation of CaCO_3 at the particle surface.

This reverse CaCO_3 formation is not observed in lime shaft kilns. These results underline the importance of considering the advective mass transport in the porous limestone particles in the simulation of lime shaft kilns. Especially when boundary conditions close to actual operating conditions are used, e.g. large particle diameters (about 6 cm) and high gas temperatures in the calcination zone (about 1400 °C), neglecting the advection would falsify the simulation results.

Based on the results from Run A another simulation with a modified limestone feeding was conducted (Run C). In this case segregation was assumed in the hopper, thus particle with greater size were placed near the kiln wall and particle with smaller size in the kiln center (see Fig. 12). The higher temperatures in the near

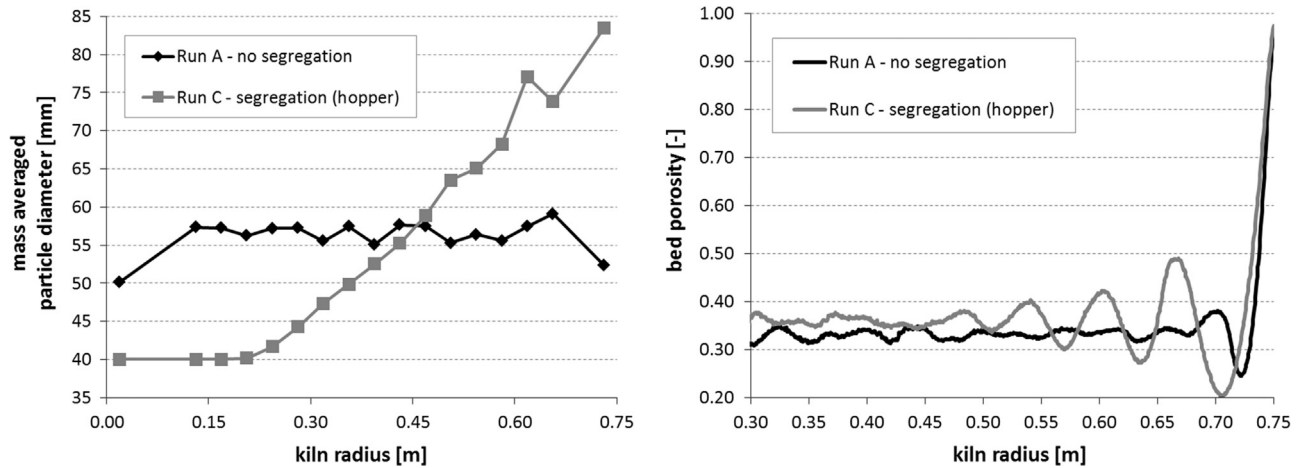


Fig. 11. Radial distribution of mass averaged particle diameter and porosity in the particle bed based on the DEM simulations.

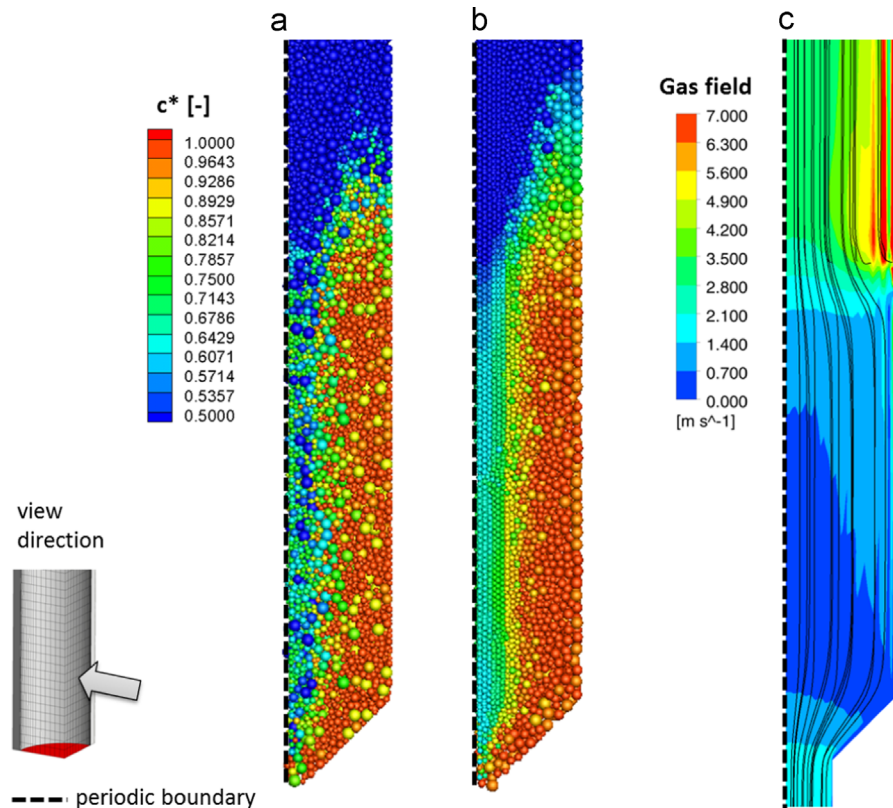


Fig. 12. Particle calcination degrees in the solid phase for Run A (left, a) and Run C (right, b) and gas field (superficial velocity) including streamlines for Run C (c).

wall region should enhance the conversion of larger particles which exhibit the lowest conversion in Run A (see Fig. 9). As shown in Fig. 11 the assumed segregation affects the local porosity and local mean particle diameter in the limestone bed. In Run A an almost constant averaged particle diameter $d_{h,p}$ and bed porosity exist due to a limestone feeding creating a strongly polydisperse bed without gradients in mean particle diameter along the radius. In Run C the bed porosity has the character of a monodisperse bed with areas of low and high porosity in the near wall region (wall effect). Thus the assumption of a constant porosity near the kiln wall is not justified and the wall affects the porosity distribution up to a wall distance of 250 mm. The radial distribution of the hydraulic particle diameter and the bed porosity are used to calculate the radial velocity profiles in the surrounding fluid phase.

The additional resistance to the flow caused by the limestone bed is described by Eq. (1) depending on the distribution of these factors.

Fig. 13 compares the distribution of the degree of calcination for the six particle classes considered in Run A with those from Run C. The modified hopper feeding leads to higher calcination degrees for the larger particle sizes. These particles classes benefit from the higher temperatures near the kiln wall leading to higher conversion degrees without changes in the residence times (see Figs. 10 and 12). Merely the classes with the two smallest particle diameters (40 mm and 50 mm) show a reduction in the degree of conversion. The majority of these particles can be found near the kiln center which is characterized by the lowest calcination temperatures. Thus the calcination degree drops compared to

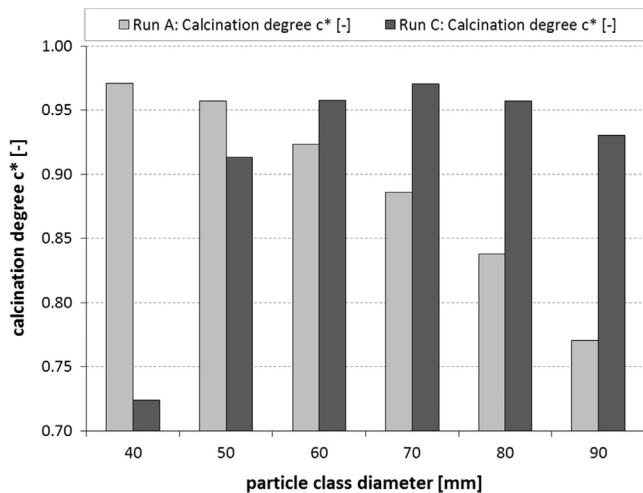


Fig. 13. Mass averaged particle calcination degree at the outlet separated according to particle size for Run A and C (sample $N=5,000$).

Run A, where this particle class is evenly distributed over the complete kiln radius. This effect is strengthened by the segregation leading to a higher hydraulic diameter and a higher bed porosity near the kiln wall. Thus the bed in the kiln center generates a higher resistance to the gas flow (Eq. (1)) and the pre-heated cooling air is forced to the kiln wall. This effect is shown in Fig. 12 by plotting the superficial gas velocity of the surrounding gas phase. The gas velocities increase towards the kiln wall due to the radial porosity distribution. Furthermore the fuel inlet through the burner ring section forces the cooling air away from the wall as shown by the streamlines in black. As a result the heating in the kiln center is reduced. However, the typical effect of a decrease in the calcination degree with an increasing particle diameter could be counteracted and a more evenly calcination degree distribution could be provided. As a result of this optimization measure the total calcination degree could be increased from 88.9% (Run A) to 91.3% (Run C).

For all runs heat and mass balances including input and output streams were carried out. The imbalances are below 4%. Thereby the energy imbalance is based on the total calcination energy and the mass imbalance is based on the total CO_2 mass flow released by the limestone bed.

5. Conclusion

The objective of this work was the development of a simulation procedure describing processes occurring in a lime shaft kiln on the system scale while taking into account detailed thermochemical processes on the particle scale affecting the reactor efficiency. The polydisperse solid phase is described by the Discrete Element Method and is coupled with a simulation of the fluid phase with CFD (ANSYS FLUENT) considering the combustion of methane injected via an annular burner section. The developed one-dimensional model for a porous spherical limestone particle describes the inner particle heat and mass transfer and their influence on the chemical conversion taking into account diffusion and advection. This model showed good agreement with experimental data for different limestone diameters.

The simulation of the vertical shaft kiln reveals significant radial temperature gradients in the calcination zone as well as in the limestone particles. Furthermore, the simulations demonstrate that advective mass transport has to be taken into account for realistic reactor behavior. The new simulation method can help to optimize the kiln design, performance and operation modes in

terms of high conversion degrees and uniform temperatures distributions. It also can be used to avoid too long residence times at high temperatures because the product quality decreases in this case due to sintering.

Nomenclature

Latin letters

a	thermal diffusivity [m^2/s]
$A_{r,m}$	exposed surface [m^2]
$A_{r,m}$	pre-exponential factor (methane reaction) [-]
A_{surf}	particle surface area [m^2]
B_{const}	constant term in the linearized species transport (CFD sided) [$\text{kg}_{\text{fluid}}/\text{m}^3/\text{s}$]
Bi	Biot number [-]
c_i	concentration of species i [kmol/m^3]
$c_{\text{CO}_2,\infty}$	equilibrium concentration [mol/m^3]
c_p	specific heat capacity [$\text{J}/\text{kg}/\text{K}$]
d_p	particle diameter [m]
$d_{h,p}$	hydraulic diameter [m]
D_i	binary bulk diffusion coefficient of species i [m^2/s]
$D_{i,j}$	binary diffusion coefficient of species i in j [m^2/s]
$D_{i,K}$	Knudsen bulk diffusion coefficient of species i [m^2/s]
$D_{i,\text{eff}}$	effective diffusion coefficient of species i [m^2/s]
E	activation energy [kJ/mol]
E_y	Young's modulus [N/mm^2]
e^n	coefficient of restitution [-]
f_e	coefficient accounting for the structure of a granular assembly [-]
\vec{F}	force vector [N]
\vec{g}	acceleration of gravity vector [m/s^2]
h	convection heat transfer coefficient [$\text{W}/\text{m}^2/\text{K}$]
H_{20}^0	enthalpy of reaction [kJ/mol]
k^n	stiffness of linear spring [kg/s^2]
k	thermal conductivity [$\text{W}/\text{m}/\text{K}$]
k_{r,CaCO_3}	chemical rate constant [m/s]
l_g	average distance length [m]
L_c	characteristic length scale [m]
m	mass [kg]
m_0	limestone mass (pure CaCO_3) [kg]
m_∞	quicklime mass (pure CaO) [kg]
\dot{m}	mass flow [kg/s]
M_j^r	rolling friction moment [N m]
\vec{M}	moment vector [N m]
M	molar mass [kg/mol]
Nu	Nusselt number [-]
p, P	pressure [Pa]
Pr	Prandtl number [-]
q	heat transfer rate [W]
r, R_p	particle radius [m]
r_c	contact radius of the circular contact zone [m]
r_i	reaction rate of reaction i [kmol/s]
r_{CH_4}	reaction rate of methane combustion [$\text{kmol}/\text{m}^3/\text{s}$]
r_{pore}	limestone pore radius [m]
R	universal gas constant [$\text{J}/\text{mol}/\text{K}$]
R_c	thermal constriction resistance [K/W]
R_g	stagnant gas zone resistance [K/W]
Re	Reynolds number [-]
Sc	Schmidt number [-]
S_e	specific surface area [m^2/kg]
$S_{i,\text{CFD}}$	mass source of species i (CFD sided) [$\text{kg}_{\text{species}}/\text{m}^3/\text{s}$]
$S_{i,R}$	net rate of production of species i by chemical reaction (DEM sided) [$\text{kg}/\text{m}^3/\text{s}$]
\vec{S}_{int}	interaction force [$\text{kg}/\text{m}^2\text{s}^2$]

Sh	Sherwood number [-]	rad	radiation
S_R	heat of calcination reaction [W/m^3]	s	solid
\vec{t}	tangential vector [-]	$surf$	particle surface
t	time [s]	$Stefan$	Species transport by Stefan flow
T	temperature [K]	$turb$	turbulent
v	velocity [m/s]	n	node (particle discretization)
V	particle volume [m^3]	N	total number of considered fluid species
$V_{c,CFD}$	CFD cell volume [m^3]		
V_n	volume of the shell (discretization) [m^3]		
\vec{x}	position vector [m]		
X	replacement character [-]		
Y_i	mass fraction of species i [kg/kg]		
$Y_{i,CFD}$	mass fraction of species i in the CFD cell [$\text{kg}_{\text{species}}/\text{kg}_{\text{fluid}}$]		
$Y_{T,C}$	correction factor [-]		

Greek letters

β_i	diffusional mass transfer coefficient of species I [m/s]
ϵ_m	emissivity [-]
ϵ	particle internal porosity [-]
θ	moment of inertia [kg/m^2]
θ_p	Poisson's ratio [-]
κ	limestone permeability (advection) [m^2]
κ_{Kn}	limestone permeability (Knudsen) [-]
γ^n	damping coefficient [kg/s]
μ	friction coefficient [-]
μ	dynamic viscosity [Pa s]
ν	[kinematic viscosity m^2/s]
ρ	density [kg/m^3]
$\rho_{f,CFD}$	fluid phase density (CFD sided) [kg/m^3]
τ	limestone tortuosity [-]
$\vec{\phi}$	angle of revolution [rad]
ϕ	porosity/void fraction [-]
$\vec{\omega}$	angular velocity vector [rad/s]
ξ	overlap [m]

Subscripts

n	normal
n	shell element index
t	tangential
t	total density
$diss$	dissipative
dyn	dynamic
el	elastic
$conv$	convection
con	conduction
$core$	particle core
$diff$	species transport by diffusion (Fick's law)
eff	lateral mixing or effective diffusion coefficient
CFD	CFD sided values
CH_4	methane
m	methane
f	fluid (CFD side)
g	gas (fluid on the DEM side)
h	hydraulic
hm	harmonic mean value
i, j, u	integral indices
lam	laminar
$Phys$	physical
p	particle
r	rolling
rf	reaction front

References

- Amritkar, A., Deb, S., Tafti, D., 2014. Efficient parallel CFD-DEM simulations using OpenMP. *J. Comput. Phys.* 256, 501–519. <http://dx.doi.org/10.1016/j.jcp.2013.09.007>.
- Aschenbach, E., 1995. Heat and flow characteristics of packed beds. *Exp. Therm. Fluid Sci.* 10, 17–27.
- Beer, F.P., Johnson, E.R., 1976. Mechanics for Engineers—Statics and DynamicsMC-Graw-Hill, New York, USA.
- Bes, A., 2006. Dynamic Process Simulation of Limestone Calcination in Normal Shaft KilnOtto-von-Guericke-Universität, Magdeburg, Germany.
- Bluhm-Drenhaus, T., Simsek, E., Wirtz, S., Scherer, V., 2010. A coupled fluid dynamic-discrete element simulation of heat and mass transfer in a lime shaft kiln. *Chem. Eng. Sci.* 65, 2821–2834. <http://dx.doi.org/10.1016/j.ces.2010.01.015>.
- Cheng, C., Specht, E., 2006. Reaction rate coefficients in decomposition of lumpy limestone of different origin. *Thermochim. Acta.* 449, 8–15. <http://dx.doi.org/10.1016/j.tca.2006.06.001>.
- Chugtai, M.Y., Michelfelder, S., 1983. Untersuchungen zur Schadstoffeinbindung durch Additiveinblasung um die Flamme. *VDI Ber.* 498, 39–55.
- Copertaro, E., Chiarotti, P., Estupinan Donoso, A.A., Paone, N., Peters, B., Revel, G.M., 2015. A discrete-continuous approach to describe CaCO_3 decarbonation in non-steady thermal conditions. *Powder Technol.* 275, 131–138. <http://dx.doi.org/10.1016/j.powtec.2015.01.072>.
- Crowe, C., Stock, D., Sharma, M., 1977. The particle-source-in cell (psi-cell) model for gas-droplet flows. *ASME Trans. J. Fluids Eng.* 99, 325–332.
- Cundall, P.A., Strack, O.D.L., 1979. A discrete numerical model for granular assemblies. *Geotechnique* 29, 47–65.
- Do, D.H., Specht, E., 2011. Determination of reaction coefficient, thermal conductivity and pore diffusivity in decomposition of limestone of different origin. In: Proceedings of the World Congress on Engineering and Computer Science.
- Fluent, 2012. FLUENT 14.0 User's Guide. Fluent Inc., Lebanon NH.
- Fuller, E.N., Schettler, P.D., Giddings, J.C., 1966. A new method for prediction of binary gas-phase diffusion coefficients. *Ind. Eng. Chem.* 58, 19–27.
- Gnielinski, V., 1978. Gleichungen zur Berechnung des Wärme- und Stoffaustausches in durchströmten ruhenden Kugelschüttungen bei mittleren und großen Peletzahlen. *Verfahrenstechnik* 21, 361–371.
- Gnielinski, V., 2006. Wärmeübertragung Partikel-Fluid in durchströmten Haufwerken. VDI-Wärmetlas. Springer-Verlag, Berlin, Germany.
- Hertz, H., 1881. Über die Berührung fester elastischer Körper. *J. Für Die Reine Und Angew. Math.* 92, 156–171.
- Hills, A.W.D., 1968. The mechanism of the termal decomposition of calcium carbonate. *Chem. Eng. Sci.* 23, 297–320.
- Jakobsen, H.A., Lindborg, H., Handeland, V., 2002. A numerical study of the interactions between viscous flow, transport and kinetics in fixed bed reactors. *Comput. Chem. Eng.* 26, 333–357. [http://dx.doi.org/10.1016/S0098-1354\(01\)00758-X](http://dx.doi.org/10.1016/S0098-1354(01)00758-X).
- Kruggel-Emden, H., Simsek, E., Wirtz, S., Scherer, V., 2007. A comparative numerical study of particle mixing on different grate designs through the discrete element method. *J. Press. Vessel Technol.* 129, 593. <http://dx.doi.org/10.1115/1.2767338>.
- Lech, R., 2007. Thermal decomposition of limestone: Part 4—permeability of product layer. *Silicon Ind.* 72, 45–52.
- Mahmoudi, A.H., Hoffmann, F., Peters, B., 2014. Application of XDEM as a novel approach to predict drying of a packed bed. *Int. J. Therm. Sci.* 75, 65–75. <http://dx.doi.org/10.1016/j.ijthermalsci.2013.07.016>.
- Mahmoudi, A.H., Hoffmann, F., Peters, B., 2014. Detailed numerical modeling of pyrolysis in a heterogeneous packed bed using XDEM. *J. Anal. Appl. Pyrolysis* 106, 9–20. <http://dx.doi.org/10.1016/j.jaatp.2013.12.001>.
- Moropoulou, A., Bakolas, A., Aggelakopoulou, E., 2001. The effects of limestone characteristics and calcination temperature to the reactivity of the quicklime. *Cem. Concr. Res.* 31, 633–639. [http://dx.doi.org/10.1016/S0008-8846\(00\)00490-7](http://dx.doi.org/10.1016/S0008-8846(00)00490-7).
- Nijemeisland, M., Dixon, A.G., Stitt, E.H., 2004. Catalyst design by CFD for heat transfer and reaction in steam reforming. *Chem. Eng. Sci.* 59, 5185–5191. <http://dx.doi.org/10.1016/j.ces.2004.07.088>.
- Peters, B., Dziugys, A., 2014. Evaluation of heat transfer on a backward acting grate. *Mechanika* 20, 27–34. <http://dx.doi.org/10.5755/j01.mech.20.1.3775>.
- Rickelt, S., Sudbrock, F., Wirtz, S., Scherer, V., 2013. Coupled DEM/CFD simulation of heat transfer in a generic grate system agitated by bars. *Powder Technol.* 249, 360–372. <http://dx.doi.org/10.1016/j.powtec.2013.08.043>.
- Satterfield, C.N., Sherwood, T.K., 1963. The Role of Diffusion in Catalysis. Addison-Wesley, London.
- Senegačnik, A., Oman, J., Širok, B., 2008. Annular shaft kiln for lime burning with kiln gas recirculation. *Appl. Therm. Eng.* 28, 785–792. <http://dx.doi.org/10.1016/j.applthermaleng.2007.04.015>.

- Shagapov, V.S., Burkin, M.V., 2008. Theoretical modeling of simultaneous processes of coke burning and limestone decomposition in a furnace. *Combust. Explos. Shock Waves* 44, 55–63.
- Shi, D., Vargas, W.L., McCarthy, J.J., 2008. Heat transfer in rotary kilns with interstitial gases. *Chem. Eng. Sci.* 63, 4506–4516. <http://dx.doi.org/10.1016/j.ces.2008.06.006>.
- Simsek, E., Wirtz, S., Scherer, V., Kruggel-Emden, H., Grochowski, R., Walzel, P., 2008. An experimental and numerical study of transversal dispersion of granular material on a vibrating conveyor. *Part. Sci. Technol.* 26, 177–196. <http://dx.doi.org/10.1080/02726350801903772>.
- Simsek, E., Brosch, B., Wirtz, S., Scherer, V., Krüll, F., 2009. Numerical simulation of grate firing systems using a coupled CFD/discrete element method (DEM). *Powder Technol.* 193, 266–273 <http://dx.doi.org/10.1016/j.powtec.2009.03.011>.
- Stark, J., Wicht, B., Zement und Kalk, Birkhäuser, Weimar, 2000.
- Sudbrock, F., Kruggel-Emden, H., Wirtz, S., Scherer, V., 2015. Convective drying of agitated silica gel and beech wood particle beds - experiments and transient DEM-CFD simulations just acce. *Dry. Technol.*
- Takkinen, S., 2012. Heat and mass transfer in calcination of limestone particles 58, 2563–2572. <http://dx.doi.org/10.1002/aic> Alche J. 58, 2563–2572. <http://dx.doi.org/10.1002/aic>.
- Vargas, W.L., McCarthy, J.J., 2002. Conductivity of granular media with stagnant interstitial fluids via thermal particle dynamics simulation. *Int. J. Heat Mass Transf.* 45, 4847–4856. [http://dx.doi.org/10.1016/S0017-9310\(02\)00175-8](http://dx.doi.org/10.1016/S0017-9310(02)00175-8).
- Vonderbank, R.S., Leithner, R., Schiewer, S., Hardow, B., 1993. Modellierung paralleler Kalzinierung und Sulfatierung bei der SO₂-Einbindung durch das Trocken-Additiv-Verfahren. *Brennstoff Warme Kraft.* 45, 443–450.
- Yagi, S., Kunii, D., 1957. Studies on effective thermal conductivities in packed beds. *AIChE J.* 3, 373–381.
- Zogg, M., 1983. *Wärme- und Stofftransportprozesse: Grundlagen und Einheitsoperationen der thermischen Verfahrenstechnik*, 1. Auflage, O. Salle Verlag, Frankfurt am Main, Berlin; München.